NANO LETTERS

2007
Vol. 7, No. 5
1213−1219

Dipole–Dipole Interactions in Nanoparticle Superlattices

Dmitri V. Talapin* and Elena V. Shevchenko

The Molecular Foundry, Lawrence Berkeley National Laboratory, Berkeley, California 94720

Christopher B. Murray

IBM Research Division, Thomas J. Watson Research Center, Yorktown Heights, New York 10598

Alexey V. Titov and Petr Král*

Department of Chemistry, University of Illinois at Chicago, Illinois 60607

Received January 9, 2007; Revised Manuscript Received February 28, 2007

ABSTRACT

Nanoparticles often self-assemble into hexagonal-close-packed (hcp) structures although it is predicted to be less stable than face-centered-cubic (fcc) packing in hard-sphere models. In addition to close-packed fcc and hcp superlattices, we observe formation of nonclose-packed *simple-hexagonal* (sh) superlattices of nearly spherical PbS, PbSe, and γ-Fe_2O_3 nanocrystals. This surprisingly rich phase diagram of monodisperse semiconducting nanoparticles is explained by considering the interactions between nonlocal dipoles of individual nanoparticles. By calculating the total electrostatic and dispersive energies, we explain stability of the hcp and sh nanoparticle superlattices, introduce the superlattice phase diagram, and predict antiferroelectric ordering in dipolar nanoparticle superlattices.

Self-assembly is the fundamental phenomenon that generates structural organization on all length scales. Among the variety of objects that can self-assemble into ordered structures, uniform spheres are the simplest model system. Ordering of spherical particles has been extensively studied both theoretically and experimentally.[1−3] Entropy can drive the ordering of noninteracting hard spheres because of the increased local free space available for each sphere in the ordered lattice compared to the disordered state.[1] Theoretical calculations and simulations of hard-sphere colloids predict that the fcc structure should be slightly more stable compared to the hcp structure.[2,3] The free energy difference between these two structures with identical packing density (∼0.7405) is very small, about $\sim 10^{-3}\ k_B T$ per particle.[2,3] In agreement with this prediction, monodisperse micron-size latex and silica spheres, whose behavior is similar to hard spheres, exhibit predominantly fcc superlattices, also known as synthetic opals,[4] whereas the hcp phase does not form.[4,5] Formation of the fcc synthetic opals is both thermodynamically and kinetically favored.[4]

We study the self-assembly of nearly spherical monodisperse particles in the sub-10 nm size range where electronic structure and magnetic properties are strongly dependent on particle sizes.[6] The resulting nanoparticle superlattices constitute a novel type of "artificial solids", with properties determined both by individual nanoparticle building blocks and collective interactions.[7] Recent studies demonstrated the enormously rich phase variety of binary nanoparticle superlattices,[8,9] which goes far beyond the predictions of hard sphere models.[10] The goal of this study is to provide a better understanding of parameters that govern self-assembly of nanoscale objects and could be used to engineer nanoparticle superlattices structure and properties.

Monodisperse colloidal nanocrystals tend to pack into ordered superlattices during slow evaporation of carrier solvent[6] or gentle destabilization of the colloidal solution.[11] The lateral size of crystalline domains varies from several superlattice unit cells to hundreds of microns, depending on experimental conditions such as particle size distribution, solvent evaporation rate, etc.[11,12] Previous studies demonstrated that nanoparticles can organize themselves into a variety of ordered structures including chains,[13,14] rings,[14] and free-floating sheets.[15] Formation of hcp superlattices is rather common in the case of both semiconductor (e.g., CdSe) and magnetic (e.g., $CoPt_3$) nanoparticles, as shown in Figure 1. hcp packing with characteristic ABAB-type stacking of hexagonally packed nanocrystal layers schematically shown in Figure 1c was observed both in thin films (Figure 1a,b)

* Corresponding authors: E-mail: dvtalapin@lbl.gov (D.V.T.); pkral@uic.edu (P.K.).

10.1021/nl070058c CCC: $37.00
Published on Web 03/31/2007

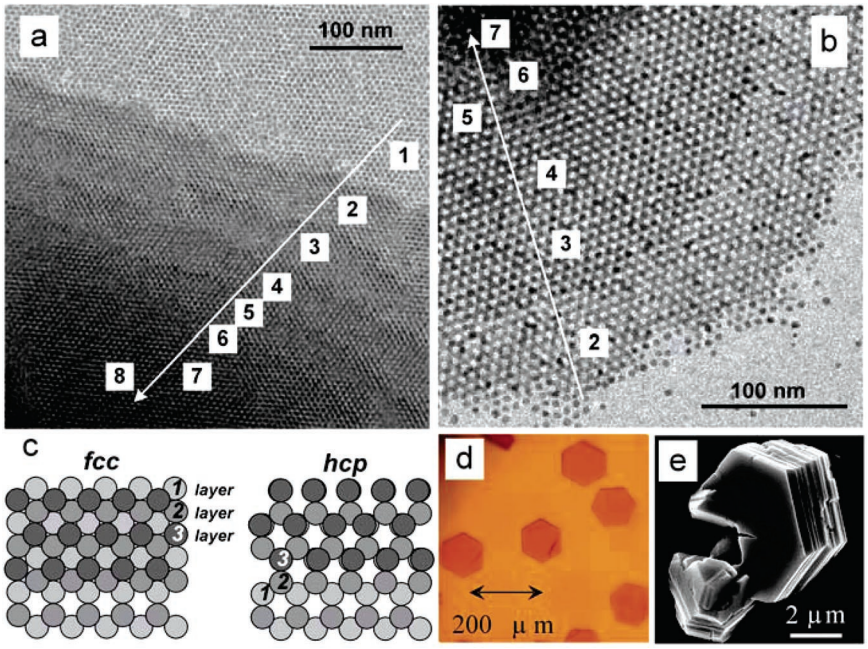

Figure 1. Nanoparticle superlattices with hcp packing symmetry. (a) TEM image of [111] projection of a superlattice self-assembled from CdSe nanocrystals. The numbers highlight nanocrystal layers with ABAB... layer stacking, characteristic to the hcp lattice. (b) TEM image of an [111] projection of hcp superlattice self-assembled from $CoPt_3$ nanocrystals. (c) Scheme showing the difference between [111] projections of fcc and hcp packing. (d) Optical micrograph of macroscopic 3D superlattices of CdSe nanocrystals faceted as hexagonal platelets, typical for hcp lattice. SEM image of self-assembled hexagonal nanoplate is shown in Figure S1 in Supporting Information. (e) SEM image of 3D superlattice of $CoPt_3$ nanocrystals. Details on nanocrystal synthesis and assembly can be found in refs 11 and 12.

and macroscopic 3D "supercrystals" (Figure 1d,e). We have observed hcp packing in superlattices of CdSe, $CoPt_3$, InAs, γ-Fe_2O_3, Co, FePt, and other nanocrystals. Often hcp and fcc superlattices form simultaneously, however, hcp packing clearly dominates over fcc under certain experimental conditions (e.g., Figure 1d). In the self-assembly of these nanoparticles, additional forces should play a substantial role because traditional models of entropy-driven hard-sphere assembly would only anticipate fcc structure.[2,3]

The structures formed from larger and more polar nanoparticles are even more striking. We find that nearly spherical PbSe and PbS nanocrystals with diameters above ~7 nm often self-assemble into superlattices shown in Figure 2. Instead of growing layer-by-layer (Figure 1a,b), these structures form abrupt boundaries with the unstructured phase. The superlattice is at least three nanocrystals thick, even near the edge of ordered domain, as seen from the image contrast in Figure 2a. Diffraction of electrons in a column of nanocrystals with mutually rotated atomic lattice planes gives rise to rotational moiré fringes, seen in Figure 2b. Figure 2c shows a corresponding high-resolution image. All these data confirm the nanocrystals in the superlattice are arranged in hexagonally ordered vertical columns producing a *simple hexagonal* (sh) structure, space group *P*6/*mmm*. The nanocrystals form layers with hexagonal ordering, and these layers assemble one-on-one in the vertical direction (i.e., AAA-type layer stacking). We observed sh type superlattices in assemblies of PbSe, PbS, and γ-Fe_2O_3 nanoparticles (Figures S2 and S3 from Supporting Information). Details on nanoparticle synthesis and assembly are given in the Supporting Information.

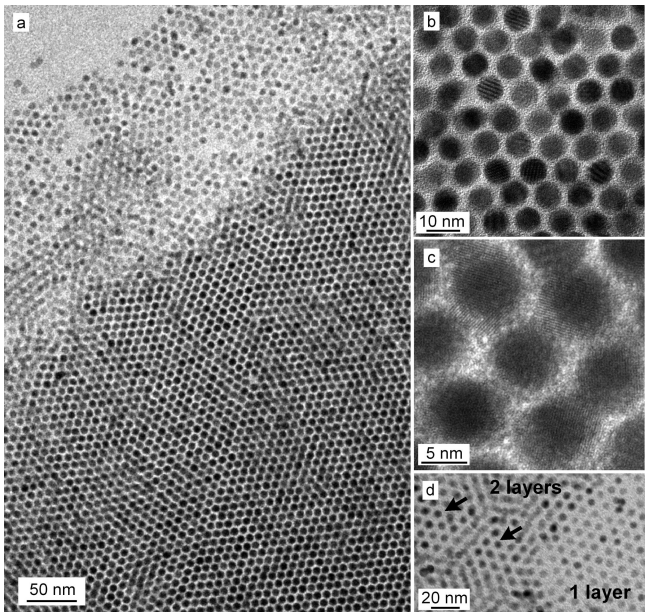

Figure 2. Superlattices of 7.2 nm PbSe nanocrystals. (a) Overview TEM image showing interface between superlattice and unstructured phase. (b) TEM image showing moiré fringes originating from the diffration of electrons on nanocrystals with mutually rotated atomic planes and (c) corresponding high-resolution TEM image. (d) TEM image showing formation of the second layer of PbSe nanoparticles with AA layer stacking (i.e., directly above the particles from the first layer). Arrows show hexagonally ordered nanocrystal columns.

Similar hexagonal ordering of nanoparticles could in principle also correspond to the [011] projection of the fcc lattice.[16] However, in the [011] projection of the fcc lattice, the hexagons are stretched by ~15% along the [0$\bar{1}$1]

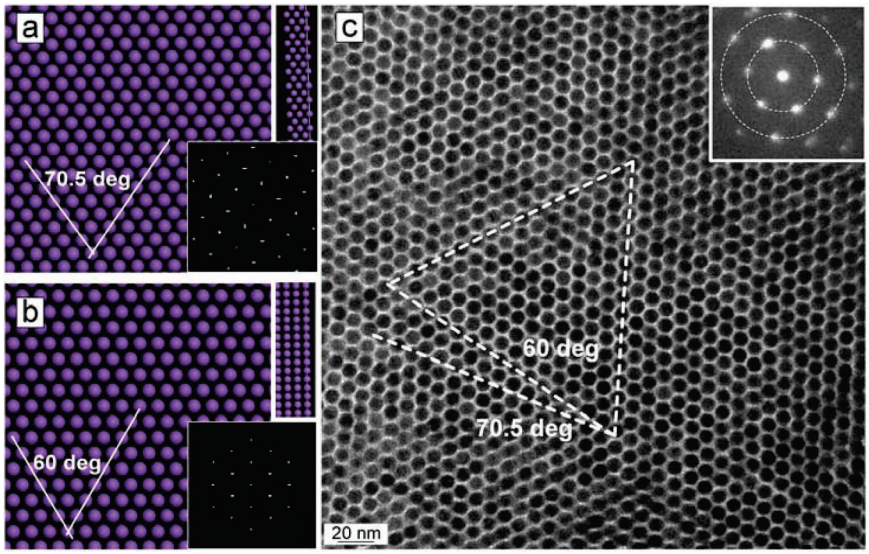

Figure 3. (a,b) Modeled (a) [011] projection of fcc lattice and (b) [001] projection of *simple hexagonal* (sh) lattice, respectively. Right bottom insets show FFT of these lattice projections with (a) 2-fold and (b) 6-fold rotational symmetry, respectively. Right top insets show side view of the superlattices. (c) TEM image of 7.2 nm PbSe nanocrystal superlattice. The angle between superlattice planes is 60°, typical for sh lattice. The inset shows small-angle electron diffraction pattern collected from 6 μm^2 superlattice area.

direction, as shown in Figure 3a. The reduced, 2-fold rotational symmetry of the superlattice is reflected in the FFT pattern through the difference of the lattice parameters along [200] and [111] directions. The angle between [111] and [1$\bar{1}$1] planes of the fcc lattice is 70.5°,[16] whereas the angle between planes in the hexagonal lattice should be 60° (Figure 3b). The PbSe nanocrystal superlattice exhibits an undistorted hexagonal arrangement of nanocrystal columns, with the angles between the lattice planes very close to 60° (Figure 3c). Fourier analysis of TEM images and selected area electron diffraction collected from a 6 μm^2 area confirm 6-fold rotational symmetry of the superlattice projection. Analysis of many TEM images of PbSe and PbS nanocrystal superlattices gives the average deviation in lattice constant of about 6%, which is significantly smaller than that expected for [011] projection of fcc lattice. These small, local superlattice distortions could be induced by nanocrystal size distribution, point defects, or inhomogeneities in dipole orientations of the nanoparticles. We observed similar distortions of hexagonal packing in the first layer of PbS and PbSe nanocrystal superlattices. Analysis of the edges of superlattice domains revealed the early stages of superlattice formation (Figure 2d). In the second layer, sh packing competes with fcc and hcp structures. Relative stability of the sh lattice compared to the close-packed structures increases with the number of layers, as seen in Figure 2a. Figure 2d also demonstrates that the superlattices shown in Figure 2 cannot be the [111] projection of six-layer-thick bcc structure. The analysis of bcc lattice is given in Supporting Information (Figure S4).

To the best of our knowledge, the sh structure has not been reported for superlattices of spherical nanoparticles or opals. Moreover, stability of the sh lattice has not been predicted by theoretical calculations or simulations of hard sphere colloids. Formation of the nonclose-packed sh superlattice would be possible due to additional directional interparticle interactions. Our previous studies of binary nanoparticle systems show that the behavior of nanoparticles differs substantially from that predicted for hard spheres because of strong Coulombic, charge−dipole, dipole−dipole, and dispersive (van der Waals) interactions.[8,9]

The sh lattice could be stabilized by anisotropic interactions between dipolar nanoparticles. Semiconductor nanocrystals are known to have large dipole moments, which can generate chaining of nanoparticles in solution.[13,14] Analogously, magnetic nanoparticles can form chains in magnetotactic bacteria.[17] In nanoparticles with wurtzite structure (e.g., CdSe), an electric dipole moment originates from the noncentrosymmetric atomic lattice and scales with the nanoparticle volume.[18,19] Moreover, both experimental and theoretical studies demonstrated large dipole moments for nanoparticles with centrosymmetric zinc blend (ZnSe, CdTe) and rock salt (PbSe) lattices. In such nanoparticles, dipole moments can originate from noncentrosymmetric distribution of polar facets around the nanocrystal[14] or asymmetric lattice truncations.[18,20] Assuming a random distribution of polar facets around a cuboctahedral PbSe nanocrystal, almost 90% nanocrystals with supposedly centrosymmetric lattice should possess permanent dipole moments.[14]

In our modeling, we calculate the cohesive energies of the fcc, hcp, and sh nanoparticle superlattices in the presence of dipolar and dispersive (van der Waals) interactions but exclude monopolar Coulombic interactions because superlattices of charged monodisperse nanoparticles cannot be neutral. We consider spherical nanoparticles with diameters that are close to those used in the experiments. The interactions between nanoparticles are described by effective potentials reflecting typical microscopic interactions. Most previous theoretical studies of dipolar micro- and nanoparticles used the model of *point dipoles* (e.g., ref 5 and references therein). The approximation of point dipoles is valid only if the distance between interacting dipoles is much

larger than the actual dimensions of the dipoles.[21] Recently, Sinyagin et al. used more accurate form of the interparticle potential to describe electrostatic interaction between nanoparticles.[22] The analytical form of electrostatic potential between two spherical particles was originally developed for dilute polyelectolyte solutions and took into account the nonlocal charge distribution effects, however, it showed significant errors at small interparticle separations, especially in the presence of dielecric discontinueties at the particle boundaries.[23] This is not appropriate for a superlattice of semiconductor nanoparticles, where the length of the dipoles exceeds the interparticle distances. Because the dipole moment in PbSe nanoparticles is associated with noncentrosymmetric distribution of charges at the nanoparticle surface,[14] we describe the *nonlocal dipoles* by two opposite point charges $\pm q$ symmetrically placed on the opposite sides (surfaces) of the nanoparticle. The interactions between the point charges of different nanoparticles are described by the Coulombic potentials,

$$V_{mn}^{C} = \frac{q_m q_n}{4\pi\,\epsilon_0 \epsilon\, r_{mn}} \tag{1}$$

where r_{mn} is the distance between mth and nth point charge, q_m denotes the charge of the mth point charge at the nanoparticle, ϵ_0 is vacuum permittivity, and ϵ is the dielectric constant ($\sim$2.0 for the interparticle medium and above 100 for PbSe nanocrystal core[24]). The interparticle medium is formed by long hydrocarbon chains of capping ligands such as oleic acid and trioctylphosphine. Depending on the ordering of hydrocarbon chains, the dielectric permittivity of hydrocarbon layer can vary from about 1.9, typical for disordered hydrocarbon molecules, to 2.5, reported for perfectly ordered self-assembled monolayers (SAMs).[25] The hydrocarbon chains on a curved nanoparticle surface are highly disordered, and their effective dielectric permittivity is close to 2.0; this value is commonly used in STM and charge transport studies on semiconductor nanoparticles.[7,26] We model the effect of the dielectric constant by using effective charges and neglect screening by any possible free charges in the system.

The van der Waals potential between two spherical particles is described as[27−29]

$$V_{ij}^{vdW} = -\frac{A}{12}\left\{\frac{R}{D_{ij}[1 + D_{ij}/4R]} + \frac{1}{1 + D_{ij}/R + D_{ij}^{2}/4R^{2}} + 2\ln\left(\frac{D_{ij}[1 + D_{ij}/4R]}{R[1 + D_{ij}/R + D_{ij}^{2}/4R^{2}]}\right)\right\} \tag{2}$$

Here, $R = d/2$ is the nanoparticle radius, D_{ij} is the distance of the closest approach between ith and jth nanoparticles (for the nearest neighbors $D_{ij} \sim 1-2$ nm), and A defines the Hamaker constant. The calculated and measured values of the Hamaker constant for semiconductor nanoparticles interacting across a hydrocarbon layer vary widely with the material. For example, $A \sim 0.1$ eV for CdS interacting across hexane[30] and $\sim$0.3 eV for a CdSe/hexane/CdSe system.[31] The Hamaker constants for PbS in vacuum is about 25% smaller than that of CdS,[32] and A for PbS/hexane/PbS interaction can be estimated as $\sim$0.04 eV,[33] whereas for PbSe/hexane/PbSe, $A \sim 0.15$ eV.[34]

The expression for the total binding energy can be written as

$$E_{tot} = \frac{1}{2}\sum_{m\neq n}^{2N}\frac{q_m q_n}{4\pi\,\epsilon_0 \epsilon\, r_{mn}} + \frac{1}{2}\sum_{i\neq j}^{N} V_{ij}^{vdW} + V_{rep} \tag{3}$$

where, in the first term, we sum only the charges located in different nanoparticles. Assuming that the charge-separation distances within each dipole are equal to the particle diameter d, the charges in the dipoles are chosen so as to fit the dipole's strength estimated from the experiment[18,19,35] (e.g., $\mu = 100$ D for $d = 5.8$ nm CdSe NPs). We do not have direct experimental data for dipole strengths in PbSe nanocrystals, but the efficient formation of PbSe nanoparticle chains at 250 °C gives the estimate for the dipole moments in 5 nm PbSe nanoparticles as $\mu > 125$ D.[36] We model the repulsive potential V_{rep} by a hard-core-type form that stabilizes the distances of the nanoparticles. To underline the fact that different structures are obtained for different sizes of nanoparticles, we introduce a dimensionless variable $S = R/(R + c)$, where c is the thickness of the nanoparticle surfactant shell. S can also be used to characterize the *nonlocal character* of the dipoles, when the charges are placed at the nanoparticle surfaces.

In our experiments, crystallization of nanoparticles into superlattices occurs on thin (5−15 nm) carbon layers. Free electrons in the conducting carbon substrate screen the electric field of the dipoles,[37] which leads to an additional energy term due to the Coulombic coupling of all dipoles with their mirror images that is also included in our modeling. Indeed, we experimentally observed the influence of nanoparticle−substrate interactions on the self-assembly of LaF_3 triangular nanoplates and binary nanoparticle superlattices.[8] There should be certain similarities in the behavior of dipolar nanoparticles, self-assembled monolayers (SAMs), and lipid bilayers. Similar to nanoparticles, the assembly of SAMs and lipid bilayers is affected by their dipole moments ($\sim$15 D), dielectric discontinuities (or image charges), and adsorption kinetics.[38,39]

We evaluate the total energies for different sizes of nanoparticles and their clusters on the graphitic surface to estimate the importance of the various factors that influence the self-assembly process. In further calculations, we use the following parameters: $A = 0.15$ eV, $Q = \pm 0.358$ e ($\mu = 100$ D for $d = 5.8$ nm), $\epsilon = 2$, $R = 2.9$ nm, and $c = 1$ nm, giving $S = 2.9/(2.9 + 1) = 0.74$. A single nanoparticle with the horizontally oriented dipole has the binding energy to the graphite surface of $E_{surf} = -4.7$ meV (Figure 4a). The binding energy for the nanoparticle with the vertically oriented dipole is -29.4 meV (Figure 4b); including the dielectric constant of the nanoparticle, $\epsilon > 100$, might significantly increase the binding energy in the case of

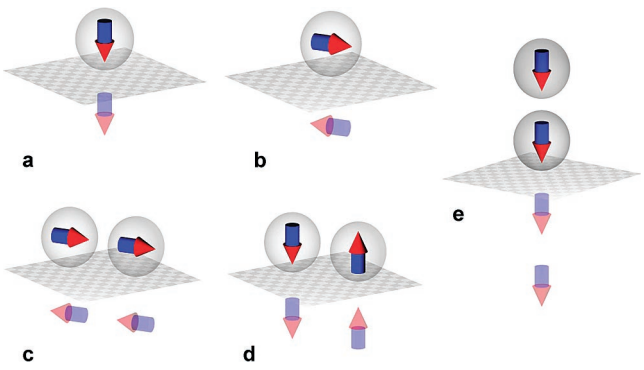

Figure 4. Typical configurations of one and two nanoparticles on the graphite surface are shown. Interaction of nanoparticles with substrate can occur through the image charges.

vertically oriented dipole. Two-particle clusters shown in the configurations from Figure 4c,d,e) have the particle−surface interaction energies of $E_{surf} = -8.2$, -57.6, and -33.7 meV, respectively. The total energies, which include mutual dipole−dipole binding of the nanoparticles are $E_{tot} = -37.6$, -62.3, and -63.1 meV for the above-discussed nanoparticle configurations, respectively. Therefore, a single nanoparticle or nanoparticle pair with parameters used in our experiments should prefer vertical rather than horizontal dipoles orientation because of the stronger electrostatic binding to the conducting substrate surface. Although these energies are close to the thermal energy $k_BT = 25$ meV at room temperatures, their values could be larger for the PbSe nanoparticles with larger dipoles. Nanoparticle crystals with binding energies per particle that are close to k_BT have been also reported.[28]

With increasing lateral dimensions of the nanoparticle clusters, the horizontal orientation of the dipoles can become energetically more preferable because of a larger mutual connectivity of dipole moments. The nucleation of the nanoparticle clusters can be a very important step in the self-assembly process. As soon as a sufficiently large cluster is formed, every new nanoparticle might join the existing arrangement of the dipoles and follow the geometrical pattern templated by the underlying lattice even if it might become less energetically favorable during the progressing self-assembly.

Next, we compare in more detail the possible structures and energies of nanoparticle clusters. The energies per particle for different clusters with three layers, each with 5 × 5 nanoparticles, are summarized in Table 1. If all nanoparticle dipoles orient in the same direction, we call such configuration *ferroelectric*; if dipole orientations alternate in the adjacent rows, we call it *antiferroelectric*. We can see that the sh lattice with vertical orientation of dipoles has the lowest energy due to relatively strong dipole−dipole coupling and interaction with the conductive substrate. The electron diffraction patterns taken from the sh superlattice of PbSe nanocrystals shown in Figures 2 and 3 are consistent with the vertical orientation of nanocrystal dipole moments, which are typically oriented along the {001} axes of PbSe nanocrystals (Figure S5, Supporting Information).[14] The role of image charges in stabilization of sh lattice was confirmed by assembling PbSe nanocrystals on insulating silicon nitride membranes. In agreement with our calculations, on the insulating substrate, PbSe nanocrystals self-assembled into fcc and hcp superlattices (Figure S6, Supporting Information).

To better illustrate these results, we show in Figure 5 three low-energy structures. The ordering of dipoles in nanocrystal superlattices results in substantial gain of binding energy and can manifest itself through preferential orientation of nanocrystals often observed in the superlattices.[6] Moreover, it can affect relative stabilities of different superlattice structures. In the close-packed fcc and hcp lattices, the horizontal orientation of dipoles is more favorable because the dipoles have a higher "connectivity" than in the vertical arrangements. Their binding to the surface is also not large, which allows easy rearrangement of particles leading to coherent lattices, as seen in Figure 1. We found that the final size of nanoparticle dipoles not only controls the *type of structure* that is formed, but it can also influence the *orientation of the dipoles*. In particular, we found that, for "short" dipoles (of the length $L_d < d/2$), the ferroelectric configuration becomes more stable than the antiferroelectric. If we introduce the ratio between the length of the dipoles and the center-to-center interparticle distance, $\sigma = L_d/2(R + c)$, we obtain that the transition between the ferroelectric and antiferroelectric lattices occurs at $\sigma_{crit} \sim 0.369$ (for the 30 × 30 three-layer hcp system).

We now select the lattice configurations with the largest total binding energies, i.e., fcc (A-H), hcp (A-H), and sh (A-V), shown in Figure 5, and search for possible transitions between hcp, fcc, and sh lattices on the graphite surface. The first somewhat counterintuitive result of dipole−dipole interactions is the higher stability hcp structure compared to fcc, resulting from more favorable dipolar coupling in the hcp packing, with odd layers sitting on the top of each other. This explains the experimentally observed formation and stability of hcp nanocrystal superlattices (Figure 1). Our calculations show a small (<1%) difference between the

Table 1. Energy Terms (in meV Per Nanoparticle) in Clusters of Dipolar Nanoparticles[a]

E [meV]	fcc A-V	fcc F-V	fcc A-H	fcc F-H	hcp A-V	hcp F-V	hcp A-H	hcp F-H	sh A-V	sh F-V	sh A-H	sh F-H
C	−4.1	9.9	−25.71	−17.8	−6.6	9.7	−25.82	−17.8	−21.95	−6.7	−25.5	−18.0
vdW	−9.4	−9.4	−9.39	−9.4	−9.4	−9.4	−9.39	−9.4	−7.10	−7.1	−7.1	−7.1
surf	−10.4	−21.3	−0.45	−6.9	−10.4	−21.4	−0.45	−7.0	−10.28	−19.6	−0.4	−6.2
total	−23.8	−20.8	*−35.55*	−34.1	−26.4	−21.0	*−35.66*	−34.3	**−39.33**	−33.5	−33.0	−31.3

[a] C, Coulombic; vdW, van der Waals; surf, electrostatic binding to the surface. Labels: fcc, hcp, sh, lattice structures; A/F, antiferroelectric/ferroelectric orientation of the dipoles; H/V, horizontal/vertical orientation of the dipoles.

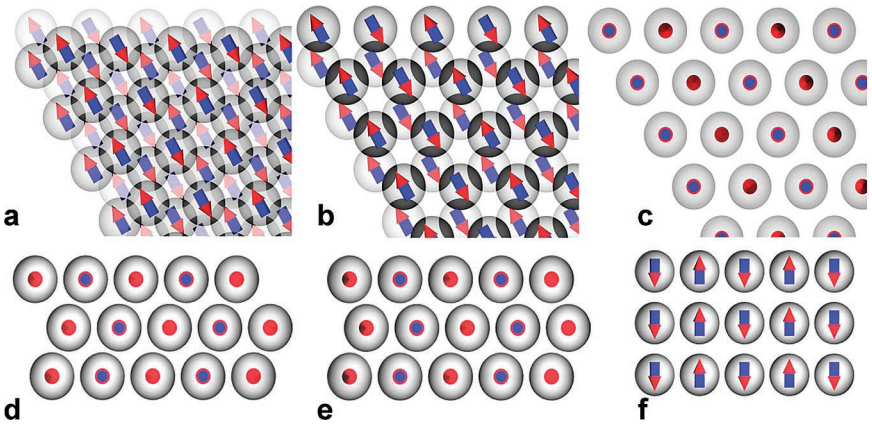

Figure 5. Dipole ordering in nanoparticle superlattices. Top view ([0001] plane) of (a) horizontal antiferroelectric ordering in fcc, (b) horizontal antiferroelectric ordering in hcp, and (c) vertical antiferroelectric ordering in sh lattices. Panels (d), (e), and (f) show side views ($[\bar{1}\bar{2}10]$ plane) of fcc, hcp, and sh structures, correspondingly.

binding energies of fcc and hcp lattices with the horizontal orientation of dipoles both for ferroelectric and antiferroelectric ordering. These results obtained for finite size thin film superlattices correlate well with the calculations of the Madelung energies for bulk fcc and hcp lattices, which predict higher stability of the hcp phase in dipolar spheres with ferroelectric ordering.[5] The Madelung energy difference between hcp and fcc, proportional to μ^2, can overcome the entropic contribution to the free energy. Because the entropic contribution to the free energy of fcc lattice is lower by $\sim 10^{-3}$ $k_B T$ per particle,[2,3] for 5.8 nm nanoparticles, the transition from fcc to hcp superlattice should occur at $\mu \sim$ 50 D at room temperature. The fcc structure should be more stable at higher temperatures, while hcp should dominate at low temperatures. This is because, in the Gibbs energy, $G = H - TS$, the advantage that hcp gets from H (enthalpy $\sim$ Coulombic energy) is cancelled at high T by the entropic term $-TS$. At $T = 0$ K, the difference of free energies G of the fcc and hcp structures is $\Delta U = C_U q^2$. Using this result, we could find the expression for the transition temperature between hcp and fcc lattices, $T_t = \Delta U/\Delta S = q^2 C_U/C_S$, where the constant C_U is given by the geometry of the lattice, and C_S is the entropic difference between the two lattices. This transition temperature determines whether the sh phase will coexist with fcc or hcp structures in a (finite temperature) phase diagram, as schematically shown in the inset to Figure 6.

In Figure 6, we show the phase diagram in the A and S (R) coordinates, where stability regions for the hcp and sh structures are shown for different surface charges $q = 0.5$ Q, Q, 1.5 Q, and 2 Q ($Q = \pm 0.358$e), corresponding to the dipole moments 50 D, 100 D, 150 D, and 200 D for the nanoparticles with the radiuses $R = 2.9$ nm. For higher accuracy, we scale the system up to three layers with 30×30 particles per layer. The sh lattice is stabilized by the Coulombic coupling to the conductive surface, which is favorable for the sh lattice. When we increase the particle size, while keeping $A =$ const and $q =$ const, the effective strength of the vdW binding (eq 2) increases. At the same time, we also increase the dipole moment, even if the charges are fixed, because the length of the dipole increases. In this

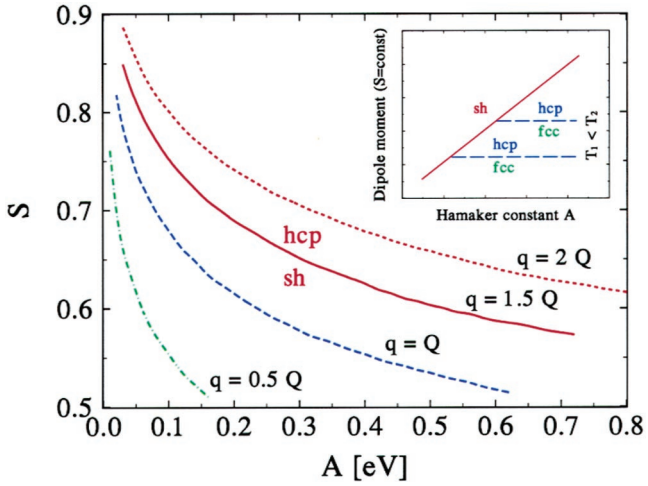

Figure 6. Phase diagrams in the coordinates $S = R/(R + c)$ vs the Hamaker constant (A) calculated for the hcp and sh lattices interacting with a conductive surface, where R and c are particle radius and thickness of the surfactant shell, respectively. Phase coexistence lines between the two phases, shown for different charges q (dipole moments of 50 D, 100 D, 150 D, and 200 D for the radius $R = 2.9$ nm). The inset schematically shows the finite temperature phase diagram of a dipolar nanoparticle superlattice taking into account Coulombic, van der Waals, and entropic contributions to the superlattice free energy.

competition, the vdW coupling can win, leading to the transition from the sh to the hcp lattice at certain S.

The data presented in Table 1 show that Coulombic dipolar interaction in semiconductor nanocrystal superlattices can be stronger than van der Waals interaction, which, in turn, can dominate over the forces associated with entropy-driven crystallization.[28]

In real nanoparlicle superlattices, the effects associated with the deviation of nanoparticle shape from spherical, partial disorder of the dipole moments or coupling of higher order multipole moments can influence the relative stabilities of fcc and hcp phases. Kinetic factors associated with solvent flow, etc., can also play important role in determining structure of nanoparticle superlattices, usually favoring the formation of fcc phase.[4] In accord with this statement, we observed formation of uniform hexagonal platelets characteristic to hcp packing of nanoparticles upon very slow

crystallization of CdSe nanocrystals, whereas faster crystallization yielded irregularly shaped superlattices with tetragonal faceting typical for fcc packing.[11] Kinetic factors can also result in formation of metastable structures such as *random hexagonal-close-packed* (rhcp) and coexistence of several structures in the same sample.[4]

Note that short-range dispersive forces favor close-packed structures, whereas dipolar interactions discussed here allow more open structures. In addition to dipoles, higher order moments of charge distribution can also affect the binding energy in nanoparticle superlattices. For example, cuboctahedral PbSe nanocrystals with eight polar ⟨111⟩ facets can possess high quadrupole and octapole moments.[14] Detailed quantitative analysis of quadrupolar and octapolar interactions goes beyond the scope of this work; however, preliminary analysis predicts that such interactions should stabilize superstructures with *simple cubic* (sc) lattice. Indeed, we often observed formation of PbSe superlattices, which could be the [001] projection of sc lattice.

In this work, we have described superlattices of monodisperse nanoparticles with dipolar interactions of nonlocal dipoles. The antiferroelectric ordering is rather unusual for bulk solids, with only a few examples observed in liquid crystals and complex oxides, e.g., $PbHfO_3$. High-resolution electrostatic force microscopy studies on nanocrystal superlattices may allow the hypothesis of antiferroelectric dipole coupling to be tested. Similar effects to those described here could also take place in superlattices of magnetic nanoparticles and greatly enrich the properties of crystalline and amorphous magnetic materials.[40] For example, collective interactions between magnetic dipoles increase blocking temperature in superlattices of magnetic nanocrystals[41] and can control their mesoscopic organization.[42] Dipolar interactions could also play important role in stabilization of particular structures of binary nanoparticle superlattices. In addition to the coupling of permanent dipoles, in binary superlattices, the electric fields generated by dipole moments of semiconductor nanoparticles can polarize metallic nanoparticles, e.g., in PbSe−Au (Ag, Pd) binary superlattices.[8,9] We are currently working on understanding dipole−dipole interactions in binary nanoparticle superlattices.

Acknowledgment. We thank H. Weller and A. Kornowski (University of Hamburg, Germany) for electron microscopy studies of CdSe nanocrystals and A. Paul Alivisatos (University of California, Berkeley) for stimulating discussions. Work at the Molecular Foundry was supported by the Director, Office of Science, Office of Basic Energy Sciences, Division of Materials Sciences and Engineering, of the U.S. Department of Energy under contract no. DE-AC02-05CH11231.

Supporting Information Available: Synthesis of PbSe nanocrystals; self-assembly of nanocrystal superlattices. This material is available free of charge via the Internet at http://pubs.acs.org.

References

(1) Alder, B. J.; Hoover, W. G.; Young, D. A. *J. Chem. Phys.* **1968**, *49*, 3688.
(2) Bolhuis, P. G.; Frenkel, D.; Mau, S.-C.; Huse, D. A. *Nature* **1997**, *388*, 235.
(3) Rudd, R. E.; Broughton, J. Q. *Phys. Rev. B* **1998**, *58*, 5893.
(4) Norris, D. J.; Arlinghaus, E. G.; Meng, L.; Heiny, R.; Scriven, E. E. *Adv. Mater.* **2004**, *16*, 1393.
(5) Hynninen, A.-P.; Dijkstra, M. *Phys. Rev. Lett.* **2005**, *94*, 138303.
(6) Murray, C. B.; Kagan, C. R.; Bawendi, M. G. *Annu. Rev. Mater. Sci.* **2000**, *30*, 545.
(7) Talapin, D. V.; Murray, C. B. *Science* **2005**, *310*, 86.
(8) Shevchenko, E. V.; Talapin, D. V.; Kotov, N. A.; O'Brien, S.; Murray, C. B. *Nature* **2006**, *439*, 55.
(9) Shevchenko, E. V.; Talapin, D. V.; Murray, C. B.; O'Brien, S. *J. Am. Chem Soc.* **2006**, *128*, 3620.
(10) Cottin, X.; Monson, P. A. *J. Chem. Phys.* **1995**, *102*, 3354.
(11) Talapin, D. V.; Shevchenko, E. V.; Kornowski, A.; Gaponik, N.; Haase, M.; Rogach, A. L.; Weller, H. *Adv. Mater.* **2001**, *13*, 1868; *Adv. Mater.* **2005**, *17*, 1325.
(12) Rogach, A. L.; Talapin, D. V.; Shevchenko, E. V.; Kornowski, A.; Haase, M.; Weller, H. *Adv. Funct. Mater.* **2002**, *12*, 653.
(13) Tang, Z.; Kotov, N. A.; Giersig, M. *Science* **2002**, *297*, 237.
(14) Cho, K.-S.; Talapin, D. V.; Gaschler, W.; Murray, C. B. *J. Am. Chem. Soc.* **2005**, *127*, 7140.
(15) Tang, Z.; Zhang, Z.; Wang, Y.; Glotzer, S. C.; Kotov, N. A. *Science* **2006**, *314*, 274.
(16) Wang, Z. L. *Adv. Mater.* **1998**, *10*, 13.
(17) Lee, H.; Purdon, A. M.; Chu, V.; Westervelt, R. M. *Nano Lett.* **2004**, *4*, 995.
(18) Shim, M.; Guyot-Sionnest, P. *J. Chem. Phys.* **1999**, *111*, 6955.
(19) Li, L.-S.; Alivisatos, A. P. *Phys. Rev. Lett.* **2003**, *90*, 097402.
(20) Shanbhag, S.; Kotov, N. A. *J. Phys. Chem. B.* **2006**, *110*, 12211.
(21) Berry, R. S.; Rice, S. A.; Ross, J. *Physical Chemistry*; Oxford University Press: Oxford, 2000.
(22) Sinyagin, A. Y.; Belov, A.; Tang, Z.; Kotov, N. A. *J. Phys. Chem. B* **2006**, *110*, 7500.
(23) Phillies, G. D. J. *J. Chem. Phys.* **1974**, *60*, 2721.
(24) Ben-Porat, C. H.; Chernyavskaya, O.; Brus, L.; Cho, K.-S.; Murray, C. B. *J. Phys. Chem. B* **2004**, *108*, 7814.
(25) Halik, M.; Klauk, H.; Zschieschang, U.; Schmid, G.; Dehm, C.; Schütz, M.; Maisch, S.; Effenberger, F.; Brunnbauer, M.; Stellacci, F. *Nature* **2004**, *431*, 963.
(26) Liljeroth, P.; Overgaag, K.; Urbieta, A.; Grandider, B.; Hickey, S. G.; Vanmaekelbergh, D. *Phys. Rev. Lett.* **2005**, *95*, 086801.
(27) Hamaker, H. C. *Physica* **1937**, *4*, 1058.
(28) Ohara, P. C.; Leff, D. V.; Heath, J. R.; Gelbart, W. M. *Phys. Rev. Lett.* **1995**, *75*, 3466.
(29) Korgel, B. A.; Fullam, S.; Connolly, S.; Fitzmaurice, D. *J. Phys. Chem. B* **1998**, *102*, 8379.
(30) Ghezelbash, A.; Koo, B.; Korgel, B. A. *Nano Lett.* **2006**, *6*, 1832.
(31) Ge, G.; Brus, L. E. *J. Phys. Chem. B* **2000**, *104*, 9573.
(32) Berngström, L. *Adv. Colloid Interface Sci.* **1997**, *70*, 125.
(33) The Hamaker constant across hydrocarbon layer (A_{121}) can be estimated from the Hamaker constant for hydrocarbon (A_{22}) and semiconductor (A_{11}) across vacuum as $A_{121} = (\sqrt{A_{11}} - \sqrt{A_{22}})^2$; Israelachvili, J. *Intermolecular and Surface Forces*: Academic Press, New York, 1992.
(34) Tang, J.; Ge, G.; Brus, L. E. *J. Phys. Chem. B* **2002**, *106*, 5653−5658.
(35) Rabani, E.; Hetényi, B.; Berne, B. J.; Brus, L. E. *J. Chem. Phys.* **1999**, *110*, 5355.
(36) Experimental observation of chaining of PbSe nanoparticles at 250 °C[14] suggests the dipolar coupling energy to be greater than k_BT at this temperature (∼0.044 eV). Using standard expressions for dipole−dipole interaction energy (see, e.g., ref 10), we can estimate the lower limit for PbSe nanoparticle dipole moment as ∼125 D.
(37) Chung, D. D. L. *J. Mater. Sci.* **2004**, *39*, 2645.
(38) Travesset, A. *J. Chem. Phys.* **2006**, *125*, 084905.
(39) McConnell, H. M.; Bazaliy, Y. B. *Proc. Nat. Acad. Sci. U.S.A.* **1995**, *92*, 8823.
(40) Závěta, K.; Jurek, K.; Kamberský, V.; Král, P.; Lachowitz, H. *J. Magn. Magn. Mater.* **1990**, *86*, 254.
(41) Murray, C. B.; Sun, S.; Doyle, H.; Betley, T. *MRS Bull.* **2001**, 985.
(42) Lalatonne, Y.; Richardi, J.; Pileni, M. P. *Nat. Mater.* **2004**, *3*, 121.

NL070058C